Progress towards WISArD

Beam line simulations and detector studies for the Weak Interaction Studies with ^{32}Ar Decay (WISArD) experiment

CERN Summer Student Report 2018

by
Lukas Nies
University of Giessen

under supervision of
Dr. Dinko Atanasov
MSc. Victoria Araujo-Escalona
KU Leuven

Geneva, September 21, 2018

Updated version, Giessen, October 5, 2018

Contents

1 Introduction

The standard model combines three out of four fundamental forces and is a well established and tested theory. Nevertheless, some phenomena, e.g. the existence of dark matter, are not predicted by the theory and therefore leave room for new physics beyond the standard model. To probe the limits of the standard model the electroweak theory offers a variety of parameters for improving current measurement precisions.

The weak interaction can not only be studied at high energies like at the LHC but also at rather low energies, for example with nuclear beta decay. Many experiments are searching for right-handed vector axial currents, exotic scalar and tensor currents, time reversal violating components, and tests of the unitary of the *CKM* matrix.

The Weak Interaction Studies with ^{32}Ar Decay (WISArD) experiment aims to measure the Doppler shifted energy spectrum of β-delayed protons from the super-allowed $0^+ \rightarrow 0^+$ ^{32}Ar decay at ISOLDE/CERN to determine a possible deviation of the angular correlation parameter $a_{\beta\nu}$ from its predicted value in the standard model.

This Summer Student 2018 project report describes the work conducted within 13 weeks in the summer of 2018 at CERN. The summer student worked full time for the WISArD experiment under the supervision of Dr. Dinko Atanasov and MSc. Victoria Araujo-Escalona (both from Katholieke Univeristeit Leuven). In this time extensive ion optics simulations were performed and silicon detectors were characterized.

1.1 Fermi theory of beta decay

Depending on the transmuting nucleus a neutron decays into a proton under emission of an electron and an anti-electron neutrino (β^- decay) or a proton decays under emission of a positron and an electron neutrino (β^+ decay). This three body decay leads to a continuous energy spectrum of the emitted leptons. The existence of a neutral particle partaking in this process was first proposed by Pauli in 1930 to solve the problem of this continuous electron (positron) spectrum and later described by Fermi as a quantum mechanical theory. Using Fermi's Golden Rule the transition rate for this process can be described by

$$\lambda = \frac{2\pi}{h} |< \Psi_f|H|\Psi_i >|^2 \frac{dn}{dE}(e^-, \bar{\nu}_e) = \frac{2\pi}{h} |M_{fi}|^2 \frac{dn}{dE} \tag{1}$$

where Ψ describes the initial and final state of the wave functions involved, H the Hamiltonian of the process, M_{fi} the matrix element, and $\frac{dn}{dE}$ the possible phase space of the two decay leptons. Considering a closed volume V one can quantize the number of states to

$$n = \frac{V}{(2\pi h)^3} \int d^3p = \frac{V}{(2\pi h)^3} 4\pi p^2 \frac{dp}{dE} \tag{2}$$

$$\leftrightarrow \frac{dn}{dE} = \frac{1}{2\pi} \frac{V}{c^3 h^7} E\sqrt{E^2 - m^2c^4} \tag{3}$$

where the relativistic energy-mass relation $E^2 = p^2c^2 + m^2c^4$ was used. Taking the attractive (repulsive) Coulomb potential of the nucleus into account the electron (positron) wave function has to be modified by the Fermi-function

$$|\Psi_e^*(0,Z)|^2 \propto \frac{1}{V}F(Z,p_e) \propto \frac{1}{V}\frac{2\pi\eta}{1-\exp^{-2\pi\eta}} \qquad \eta = \pm\frac{Ze^2}{4\pi\epsilon_0\hbar v_e} \tag{4}$$

where the positive (negative) sign is used for β^- (β^+) decay and v_e is the final velocity of the electron (positron). This leads to $F \to 1$ if the proton number Z decreases and the electron (positron) momentum p_e increases. Plugging in the results leads to the partial decay probability (detailed steps can be founds in [1]):

$$\Lambda(p_e)dp_e = \frac{|M'_{fi}|}{2\pi^3\hbar^7c^3}F(Z_D,p_e)p_e^2(E-E_e)^2\sqrt{1-\frac{m_\nu^2c^4}{(E-E_e)}}dp_e. \tag{5}$$

In Figure 1 the decay spectrum for β^+ and β^- decays are shown. If the matrix element is independent of the electron (positron) momentum and one assumes the neutrino to be massless then the decay spectrum can be expressed by

$$\sqrt{\frac{\Lambda(p_e)}{p_e^2F(Z_D,p_e)}} \propto |M'_{fi}|(E-E_e). \tag{6}$$

Plotting this quantity gives the so called Fermi-Kurie plot and enables the comparison of the shape of different beta decaying isotopes (see Fig. 2).

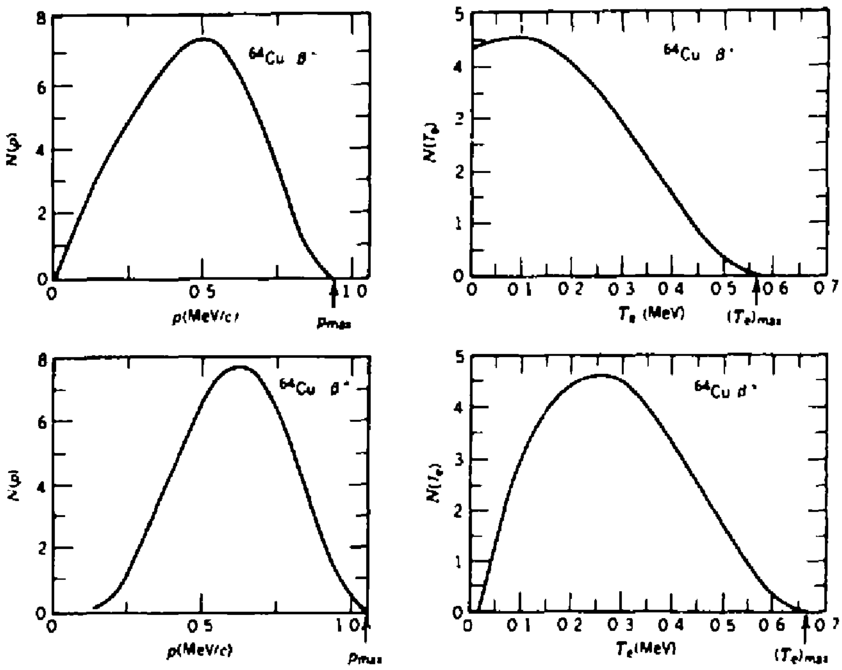

Figure 1: Energy and momentum distribution for electrons and positrons in the mixed β^- (top) and β^+ (bottom) decay of ^{64}Cu. Comparing the momenta (left) and maximum energy (right) one can find the Coulomb influence of the nucleus which leads to additional energy in the β^+ decay and reduced energy in the β^- decay. Figure taken from [1].

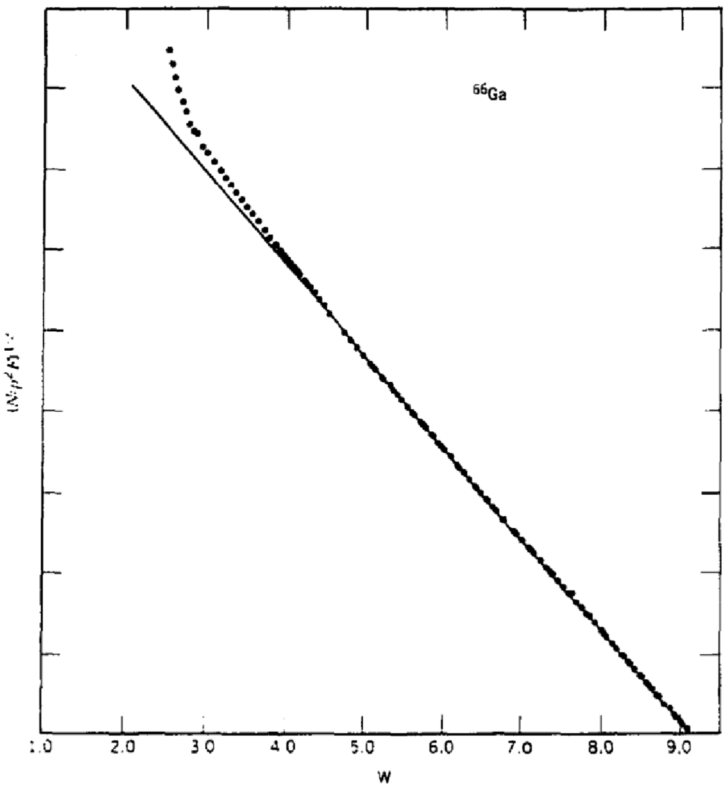

Figure 2: Fermi-Kurie plot for the ^{66}Ga β^+ decay [2]. The horizontal axis shows the relativistic total energy in units of $m_e c^2$. The deviation from the straight line results from scattering of positrons in the radioactive source.

Integrating the partial decay probability gives the total half-life

$$\lambda_\beta = \int_0^{p_e(max)} \frac{|M'_{fi}|}{2\pi^3\hbar^7 c^3} F(Z_D, p_e) p_e^2 (E - E_e)^2 dp_e = |M'_{fi}| \frac{m_0 c^4}{2\pi^3 \hbar^7} f(Z_D, E_0) \qquad (7)$$

where $f(Z_D, E_0)$ is the Fermi-integral or statistical rate function which has to be evaluated numerically. By re-ordering this result one can obtain the so called comparative half-life

$$ft_{1/2} = f\lambda_\beta^{-1} = 0.693 \frac{2\pi^3\hbar^7}{g^2|\bar{M'_{fi}}|^2 m_0^2 c^4} \approx \frac{6000}{|\bar{M'_{fi}}|^2} \qquad (8)$$

where $\bar{M'_{fi}}$ is the reduced matrix element and g the coupling strength in this particular process. Since this quantity is only dependent on the matrix element it is a good measure to compare β-decays of different isotopes.

1.2 Angular momentum and parity selection rules

The matrix element can be expressed as

$$M'_{fi} = g \int \varphi_D^*(\vec{r})_p \Psi_e^*(\vec{r}) \Psi_\nu^*(\vec{r}) \mathcal{O}(n \to p) \varphi_p(\vec{r})_n d\vec{r} \qquad (9)$$

where the operator $\mathcal{O}$ denotes the transformation from a neutron to a proton, φ_D is the wave function of the daughter nucleus, and φ_P is the wave function for the parent nucleus. Using plane waves for expressing the outgoing particles and expanding them as a power series one gets

$$M'_{fi} = g\left[\int \varphi_D^*(\vec{r})_p \mathcal{O}(n \to p)\varphi_P(\vec{r})_n d\vec{r} \right.$$
$$\left. + i(\vec{k}_e + \vec{k}_\nu)\int \varphi_D^*(\vec{r})_p \mathcal{O}(n \to p)\varphi_P(\vec{r})_n d\vec{r} + \dots\right]. \qquad (10)$$

The first term gives the overlap of initial and final state, the second term shows that the wave functions must have opposite parities. This leads to parity and angular momentum selection rules where the latter has to be conserved in any case.

One can define

$$\vec{J}_P = \vec{J}_D + \vec{J}_\beta \qquad \vec{J}_\beta = \vec{L}_\beta + \vec{S}_\beta \qquad \pi_P = \pi_D(-1)^{L_\beta} \qquad (11)$$

where $\vec{J}_P$ is the total angular momentum of the parent nucleus, $\vec{J}_D$ of the daughter, and $\vec{J}_\beta$ of the beta particle carrying away angular momentum $\vec{L}_\beta$ and intrinsic spin

Classification in β-decay

$\vec{J}_P = \vec{J}_D + \vec{L}_\beta + \vec{S}_\beta$

$\pi_P = \pi_D(-1)^{L_\beta}$

Allowed transitions	$\vec{L}_\beta = \vec{0}$
1st forbidden transitions	$\vec{L}_\beta = \vec{1}$
2nd forbidden transitions	$\vec{L}_\beta = \vec{2}$
Fermi transitions	$\vec{S}_\beta = \vec{0}$
Gamow–Teller transitions	$\vec{S}_\beta = \vec{1}$

Transition type	log fT
Superallowed	2.9–3.7
Allowed	4.4–6.0
First forbidden	6–10
Second forbidden	10–13
Third forbidden	> 15

I. Allowed transitions ($\vec{L}_\beta = 0$, $\pi_P = \pi_D$)

Fermi-type ($\vec{S}_\beta = \vec{0}$)	Gamow–Teller type ($\vec{S}_\beta = \vec{1}$)
$\vec{J}_P = \vec{J}_D$	$\vec{J}_P = \vec{J}_D + \vec{1}$
$\lvert\Delta J\rvert = 0$	$\lvert\Delta J\rvert = 0, 1$: no $0^+ \to 0^+$
$0^+ \to 0^+$: superallowed	$0^+ \to 1^+$: unique Gamow–Teller

II. 1st forbidden transitions ($\vec{L}_\beta = \vec{1}$, $\pi_P = -\pi_D$)

Fermi-type ($\vec{S}_\beta = \vec{0}$)	Gamow–Teller type ($\vec{S}_\beta = \vec{1}$)	
$\vec{J}_P = \vec{J}_D + \vec{1}$	$\vec{J}_P = \vec{J}_D + \underbrace{\vec{1} + \vec{1}}_{\vec{0}\,\vec{1}\,\vec{2}}$	
$\lvert\Delta J\rvert = 0, 1$		
no $0^- \to 0^+$	*3 types*	
	(i) $\lvert\Delta J\rvert = 0$	
	(ii) $\lvert\Delta J\rvert = 0, 1$:	no $0^+ \to 0^-$
	(iii) $\lvert\Delta J\rvert = 0, 1, 2$:	no $0^- \to 0^+$
		no $1^+ \to 0^-$
		no $\frac{1}{2}^+ \to \frac{1}{2}^-$

Figure 3: Summary of decision rules and classification for beta decays [1]. In the top right one can find corresponding ft-values.

S_β. Parity is given by the parity of the parent nucleus, π_P, the daughter nucleus, π_D and the angular momentum carried away by the beta particle. For allowed transitions it is assumed that the decay happens at $\vec{r} = 0$, hence no angular momentum can be carried away and $\pi_P = \pi_D$. In the n^{th}-forbidden decay, n angular momentum is carried away and parity changes accordingly:

$$\vec{L_\beta} = n \qquad\qquad \pi_D(-1)^n. \tag{12}$$

Despite the name, forbidden decays occur but with much lower probability. Further, two classes of decays can be defined considering the intrinsic spin carried by the electron and neutrino. In Fermi-like decays, the intrinsic spin sums to zero:

$$S_\beta = 0 \qquad \Delta J = 0 \text{ (allowed)} \qquad 0^+ \to 0^+ \text{ (super-allowed)}. \tag{13}$$

In Gamow-Teller type decays the intrinsic spin sums to one and one gets:

$$S_\beta = 1 \quad |\Delta J = 0,1| \text{ (allowed)} \quad \text{no } 0^+ \to 0^+, \text{ but } 0^+ \to 1^+ \text{ (unique Gamow-Teller)}. \tag{14}$$

The selection rules for forbidden decays get a little more complicated and can be found in Fig. 3.

1.3 Beta-delayed nucleon emission

Nuclei far off the valley of stability unstable against beta decay have a high chance not only to emit an electron or positron but also to de-excite by rapidly emitting one or more nucleons (p,n,^{4}He) if the β-decay energy is larger than the separation energy:

$$\text{Precursor} \xrightarrow{\beta^\pm} \text{Emitter} \xrightarrow{n,p,^4He} \text{Daughter} \tag{15}$$

This process competes with γ-de-excitation. Due to the involved two body process the emitted nucleons have distinct energies. The favored decay branch of the precursor towards the emitter is to its isobaric analog state (IAS). Those states are two very similar states between neighboring isobars who have a large branching ratio and a Fermi type matrix element. A transition to an IAS only changes the isospin component T_z. Therefore, if $T = T_0$ is the isospin ground state of a nucleus (N+1,Z) then the IAS in nucleus (N,$Z+1$) will be the lowest state with $T = T_0$. In Figure 17 the decay of ^{32}Ar is shown. The strongest branching ratio is the decay towards its IAS of ^{32}Cl with $T = 2$.

1.4 Exotic currents

To integrate beta-decay into the weak interaction of the standard model an adequate formulation has to be written down. A short overview is given here, for further reading see [3] and [4].

The general Hamiltonian for beta decay is given by the product of Fermi's coupling constant, G_F, and the hadronic and leptonic currents, J_H and J_L:

$$H = G_F J_H J_L = G_F \left(\bar{\Psi}_p \mathcal{O} \Psi_n\right) \left(\bar{\Psi}_e \mathcal{O} \Psi_{\nu_e}\right) + h.c., \tag{16}$$

where $\mathcal{O}$ is a quantum mechanical operator which can be expressed by combining Dirac γ-matrices. Overall 16 linear independent combinations can be grouped into five classes: scalar (S), vector (V), tensor (T), axial vector (V), and pseudoscalar (P).

In nature all five interactions occur as a linear combination:

$$H = \sum_{i=S,V,T,A,P} g_F C_i \left(\bar{\psi}_p \mathcal{O}_i \bar{\psi}_n\right) \left(\bar{\psi}_e \mathcal{O}_i \bar{\psi}_\nu\right) + h.c. \tag{17}$$

where C_i modifies the coupling constant for each case. The possibility of having odd and even terms under the parity operation and the discovery of parity violation leads to the generalized Hamiltonian:

$$\sum_i \left(H_i^{\text{even}} + H_i^{\text{odd}}\right) + h.c. = g_F \sum_{i=S,V,T,A,P} \left(\bar{\psi}_p \mathcal{O}_i \bar{\psi}_n\right) \left(\bar{\psi}_e \mathcal{O}_i \left(C_i + C_i' \gamma_5\right) \bar{\psi}_\nu\right) + h.c. \tag{18}$$

where γ_5 is the fifth Dirac matrix and prime denotes the odd terms. According to this Hamiltonian 10 coupling constants exist. At low energies, in non-relativistic treatment the pseudoscalar currents vanish. In Fermi type decays only scalar and vector type currents partake and in Gamow-Teller type decays only vector-axial and tensor currents. Parity is violated if both $C_i' \neq 0$ and $C_i \neq 0$, and maximally violated if $|C_i'| = |C_i|$. The standard model predicts $C_V' = C_V = 1$ and $C_A = C_A'$, all other coupling constants being zero. Hence, scalar, tensor, and pseudoscalar currents do not take part in the standard model.

Experiments to test this hypothesis found so far only upper limits on contributions of exotic scalar or tensor type currents in nuclear beta decay. A possible approach is considering the angular distribution of the electron (positron) and neutrino emission:

$$\begin{aligned} \omega dE_e d\Omega_e d\Omega_\nu &\propto F(\pm Z, E_e) p_e E_e (E_0 - E_e)^2 dE_e d\Omega_e d\Omega_\nu \\ &\times \xi \left(1 + a_{\beta\nu} \frac{\vec{p}_e \vec{p}_\nu}{E_e E_\nu} + b \frac{m}{E_e} + \dots\right) \end{aligned} \tag{19}$$

where the nuclear matrix element ξ is defined as

$$\begin{aligned} \xi =& |M_F|^2 \left(|C_S|^2 + |C_V|^2 + |C_S'|^2 + |C_V'|^2\right) \\ &+ |M_{GT}|^2 \left(|C_T|^2 + |C_A|^2 + |C_T'|^2 + |C_A'|^2\right), \end{aligned} \tag{20}$$

the $\beta\nu$-correlation term as

$$\begin{aligned} a_{\beta\nu}\xi = |M_F|^2 &\left[-|C_S|^2 + |C_V|^2 - |C_S'|^2 + |C_V'|^2 \mp 2\frac{\alpha Z m}{p_e} \Im\left(C_S C_V^* + C_S' C_V'^*\right)\right] \\ + \frac{|M_{GT}|^2}{3} &\left[|C_T|^2 - |C_A|^2 + |C_T'|^2 - |C_A'|^2 \pm 2\frac{\alpha Z m}{p_e} \Im\left(C_T C_A^* + C_T' C_A'^*\right)\right], \end{aligned} \tag{21}$$

and the Fierz interference term as

$$b\xi = \pm 2\gamma \Re\left[|M_F|^2 \left(C_S C_V^* + C_S' C_V'^*\right) + |M_{GT}|^2 \left(C_T C_A^* + C_T' C_A'^*\right)\right]. \tag{22}$$

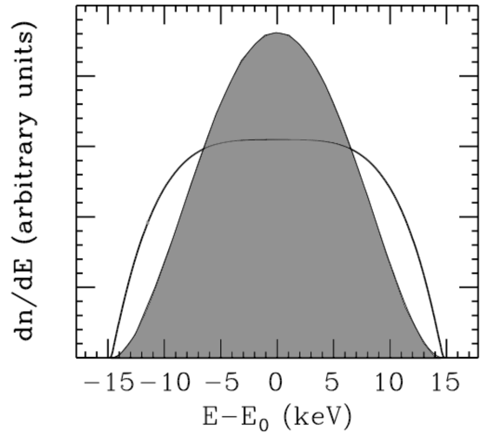

Figure 4: Energy spectrum of the $0^+ \rightarrow 0^+$ proton group from ^{32}Ar decay. The shaded curve corresponds to $a_{\beta\nu} = -1$, the other curve to $a_{\beta\nu} = +1$. Figure credits [5]

.

In the terms above M_F, M_{GT} are the Fermi and Gamow-Teller matrix elements, $\gamma = \sqrt{1-(\alpha Z)^2}$, α the fine structure constant and Z the atomic number of the daughter nucleus.

If only Fermi type decays are taken into account, maximal parity violation and time reversal invariance is assumed then the terms mentioned above simplify significantly:

$$|M_{GT}| = 0 \qquad C'_V = C_V \qquad C'_A = C_A \qquad C_V \wedge C_A \in \mathbb{R}$$

$$\xi = 2|M_F|^2 C_V^2 \tag{23}$$

$$a_{\beta\nu} \simeq 1 - \frac{|C_S|^2 + |C'_S|^2}{C_V^2} \mp \frac{\alpha Z m}{p_e} \Im \left(\frac{C_S + C'_S}{C_V} \right) \tag{24}$$

$$b \simeq \pm \gamma \Re \left(\frac{C_S + C'_S}{C_V} \right). \tag{25}$$

It is easy to see that for a small hypothetical contribution of exotic scalar currents the $\beta\nu$-correlation factor will deviate from $a_{\beta\nu} = 1$. The WISArD experiment at ISOLDE is searching for such a deviation by precisely measuring the energy of the decay products in the super-allowed $0^+ \rightarrow 0^+$ Fermi decay of ^{32}Ar.

2 The WISArD experiment

The Weak Interaction Studies with ^{32}Ar Decay (WISArD) experiment is located at the Isotope Separator On Line DEvice (ISOLDE) at CERN and will use an ^{32}Ar-ion beam delivered after mass separation by one of the two available mass separators.

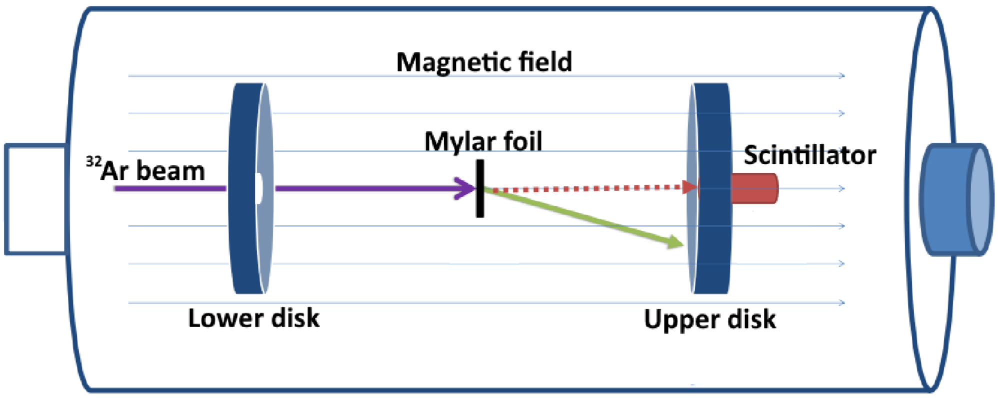

Figure 5: Schematic of the detectors. The eight silicon detectors are located on the two disks above and below the Mylar foil. The scintillator sits in the hole of the upper disk. Gravity is pointing to the left. Graphic from V. Araujo-Escalona.

2.1 Measurement principle

To measure the $\beta\nu$-correlation factor the emitted electron (positron) and the neutrino have to be detected.

Since neutrinos only interact weakly it is not feasible to build a neutrino detector for this purpose. Instead, the direction of the emitted neutrino can be reconstructed by measuring the recoil energy of the daughter nucleus. The recoil will be lower if both particles are not emitted in the same direction. Hence, a modification of the Doppler broadening of the recoil energy is expected if scalar type currents exist in the weak beta decay.

Argon ions will be continuously collected in a thin Mylar foil where they undergo β^+ decay with a half-life of 98 ms to ^{32}Cl which immediately emits a proton and therefore becomes ^{31}S (beta-delayed proton emission). The initial decay of the precursor produces a positron and an electron-neutrino with a total intrinsic spin carried away of $\vec{S}_\beta = 0$.

The recoil energy of the ^{31}Cl nucleus can be indirectly measured by measuring the proton energy. For this eight 300 µm thick silicon detectors are used. The catcher foil and the detectors are located in the cold bore of the former WITCH magnet [6]. The magnetic field can be chosen between 3 T and 9 T and channels the positrons away from silicon detectors and into a plastic scintillator which is read out by a photo diode. Background can be significantly suppressed by looking for coincident signals between detected positrons and protons.

Figure 5 shows the detector setup. The catcher foil is located between two disks each carrying four silicon detectors. The lower plate has a hole for the beam to pass through and the hole of the upper disk houses the plastic scintillator. The magnetic field lines are parallel to the beam axis.

The value for $a_{\beta\nu}$ can be extracted by comparing the resulting proton energy spectrum with Monte-Carlo simulations of different values for $a_{\beta\nu}$. This is shown in Fig. 4: if a scalar current exists and the detector resolution is sufficient one expects a small deviation from the non-shaded curve.

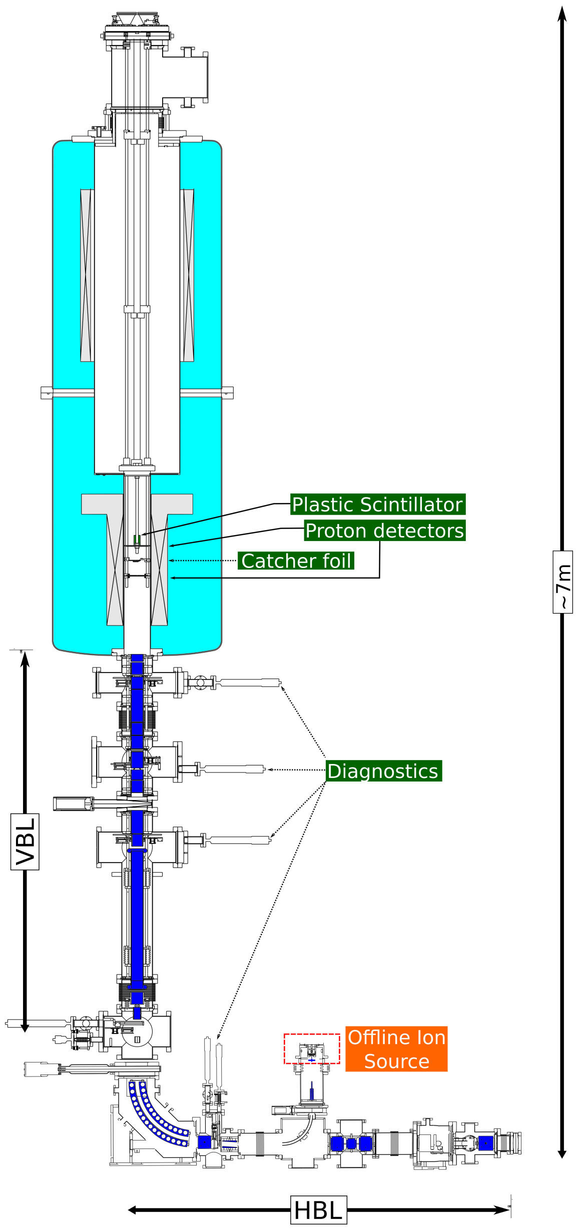

Figure 6: Schematic for the WISArD experiment. The beam line is divided in a horizontal and a vertical part.

.

2.2 Experimental setup

Due to the location of the setup in the ISOLDE facility the beam has to be transported from REXTRAP through a roughly 6 m long beam line consisting a 29° bend to the catcher foil. Since the magnetic field lines are aligned with the gravitational field lines the beam has to be bend by 90° upwards. The beam line is therefore split into a horizontal and a vertical part. For off-line beam tuning a potassium ion source is connected by a movable 90° bender to the horizontal beam line. The beam line includes several electrostatic kickers, steerers, benders, drift tubes, and einzellenses to transport the beam. Multiple Faraday cups are available to measure the beam intensity at certain positions.

The former WITCH magnet is located in a roughly 7 m high support structure which also carries parts of the vertical beam line, vacuum pumps, data acquisition, control elements, and work stations. The detector system is mounted on a 2.4 m long tower which can be lowered from the top of the magnet inside the cold bore. A graphic with descriptions is provided in Figure 6.

From the detector tower the signal cables for the silicon and scintillator detectors are fed through the top flange and are connected to preamplifiers. Additional cables for temperature sensors reading the temperature of two silicon detectors are fed through a different flange and connected to a PICO PT-104 data logger. The data acquisition system reads the data from the preamplifiers and fills an energy spectrum.

3 Summer Student Project

The summer student project was split by workload into a programming part where the student performed ion optic simulations with `SIMION` (60%) and worked hands on with detector characterizations (20%) and other lab related work (20%).

3.1 `SIMION` beam line optics simulations

The `SIMION` ion and electron optics simulation workbench is a comprehensive toolkit for simulating beam line infrastructure. It is especially capable of designing electrostatic ion optics and therefore used in many research facilities.

In this part of the project the full beam line including the WISArD offline ion source was simulated. Since the computational efficiency for carrying out the simulations depend on many factors, manly the size of the simulated parts and the symmetries, the beam line was separated into four different parts: the REXTRAP part, the ion source, the horizontal beamline, and the vertical beamline including parts of the magnet and the detector tower. Available steerers were not included in the simulations

The goal of this simulation was to optimize the beam transport quality and the beam current received on the catcher foil in preparation for the experiment beam time. To find valid electrode voltages two consecutive searches were performed: an initial "Monte-Carlo"-like parameter search to find good values for starting a

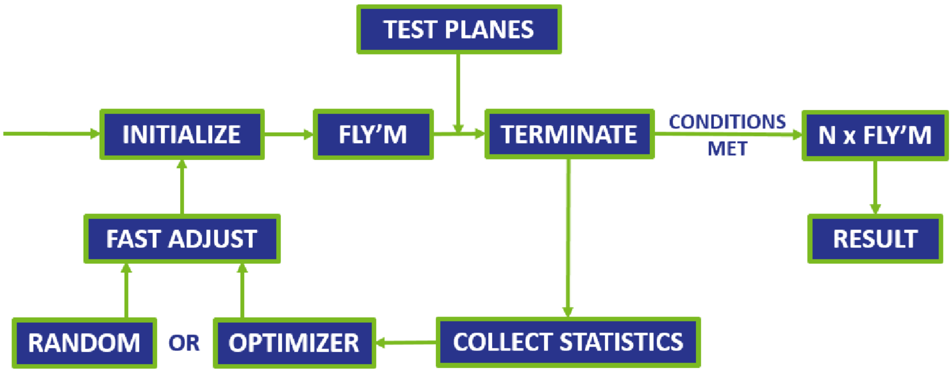

Figure 7: Schematic of the `LUA` routine.

local downhill optimizer which further looked for an optimal set of voltages. Both approaches will be shortly discussed in the following.

`LUA` routine in `SIMION`

For carrying out the random parameter search and performing further optimization a routine was written in `LUA` language. In diagram 7 this program is visualized.

The main part of the routine consists of a loop in which a certain number of ions are flown through the beam line ("Fly'm"). For each of those runs the initialization sets the conditions, e.g. electrode voltages. While the run is executed several test planes record phase space information and other characteristics at different locations in the beam line. After the run terminates those informations are collected and recorded. The metric is calculated and fed to the optimizer. The electrodes get updated by the fast adjust function depending on which method is used: either the parameter search is carried out by randomly choosing voltages or the Nelder-Mead algorithm sets the values. Following, the next run is initialized and a new loop begins.

This routine is broken if either the desired number of tests for the random search is carried out or the optimizer converges. Then the "Fly'm" is executed N times to collect statistics for the final result.

Random parameter search

For a multidimensional parameter space it is a reasonable approach to randomly pick values from a constrained set of voltages to broadly scan the surface of the metric function to optimize.

An example for the horizontal beam line part is shown in Figure 8: for three different voltages (the two benders and the kicker in the horizontal beam line) random voltages were tested. To visualize the metric function value with respect to all three electrodes at the same time, the ratio between the horizontal 90° bender and the kicker vs. the ion source bender is plotted and the metric is color coded. One can clearly see that only for a certain region good values can be achieved. The ratio scales roughly linearly with the ion source bender voltage.

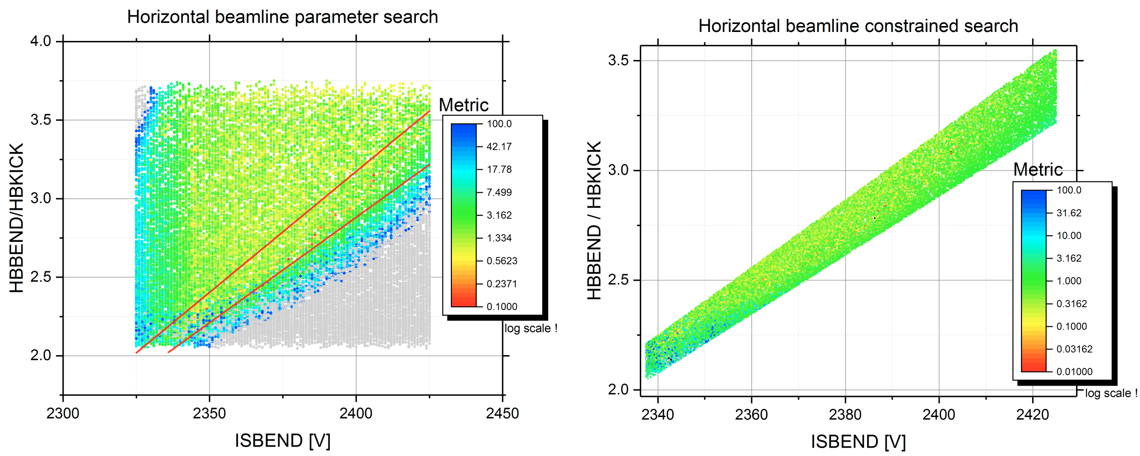

(a) Rough search (b) Constrained search

Figure 8: Example for the rough search (left) and the constrained search (right) for the two benders and the kicker in the horizontal beam line between ion source and vertical beam line. The two red lines show the boundaries set after the rough search was carried out. The metric is color coded where red-ish colors denote small and therefore good values.

This parameter search was performed for all four beam line parts in the same manner. For the search with the downhill algorithm the starting point was set into the center of the constrained space and the step size was given by the boundaries of the constrained area.

Nelder-Mead Algorithm

Once the starting point for the optimizer search was chosen by the random parameter search the Nelder-Mead algorithm was used to perform the optimization.

Here a rough sketch of the procedure [7]: consider a function $f : \mathbb{R}^n \to \mathbb{R}$ with n being the dimension of the parameter space and $X \subseteq \mathbb{R}^n$ being a possible solution in the solution space. The algorithm then constructs $n + 1$ dimensional regular simplexes, if $n = 2$ this equals a regular triangle with three vertices.

The function f is evaluated at each of the $n+1$ points. The vertex with the worst function value is excluded and replaced by it's mirror vertex (a $n = 2$ visualization is shown in Figure 9) where the "mirror plane" is given by connection between the remaining vertices.

Depending on the function value of this mirror vertex a new vertex point is calculated to generate a new simplex for the next iteration. One of five possible actions is performed to generate the new point: an expansion, a reflection, an inside or outside contraction, or a shrink.

For the next iteration the function is evaluated at each vertex and the algorithm generates a new mirror vertex or terminates if the stopping conditions are met.

As described before, to generate a set of starting points a random search was performed. After the parameter space was constrained sufficiently the Nelder-Mead algorithm was used to find a local optimum. Usually the routine converged after a

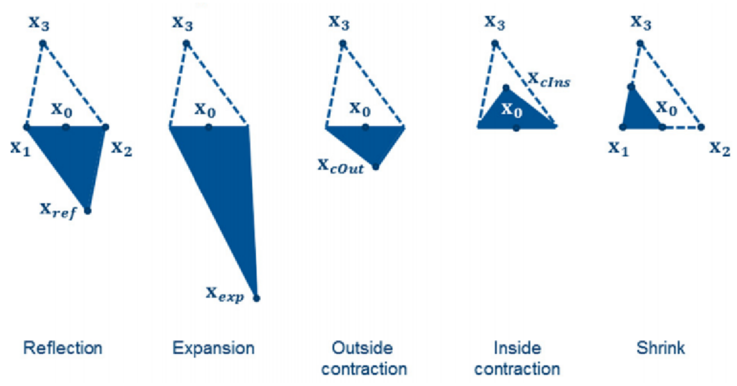

Figure 9: Two dimensional visualization for the different iteration actions of the Nelder-Mead algorithm.

couple of hundred iterations. All following results were generated by using a set of solutions given by the Nelder-Mead optimization.

Ion-source simulation

The offline ion-source of WISArD consists of a carbon cone filled with potassium powder which is heated by a current of 30 A. The source itself is floated with a high voltage to generate the necessary 30 keV beam energy. The ions are extracted by an extraction electrode and focused into a movable 90° bender. Pictures from the simulations can be found in Fig. 18.

The ions were generated with an Maxwell-Boltzmann like energy distribution between 0 eV and 7 eV where the mass of the distribution was roughly 1.5 eV. The particles were emitted in a randomly distributed cone with an solid angle between 0° of 15°. The origin of the particles was a randomly filled circle with a radius of 2 mm perpendicular to the beam axis.

In Figure 10 (top row) the results for the optimization process for the ion source is depicted. The beam profile is symmetric and shows a Gaussian profile with a standard deviation of roughly $\sigma = 1.2$ mm. The emittance is about $\epsilon = 2.3\,\mathrm{mm} \times \mathrm{mrad}$. Due to the positive inclination of the phase space plot the beam is diverging when leaving the ion source. This can not be compensated by the einzellens which is currently limited by the power supply.

Horizontal beam line

Recording the beam characteristics from the previous section and creating new particles in this section of the `SIMION` simulation the beam was transported through the movable ion source bender, the kicker, and eventually bend back towards the vertical axis by the fixed bender.

In Figure 10 (bottom row) the result for the second part of the simulation shows that, due to a lack of focusing elements, the beam is still diverging. The horizontal axis (z-axis) is not affected by the bending and kicking and therefore diverges freely up to a beam size of $\sigma_z = 7.1$ mm. The y-axis on the other side is affected by the

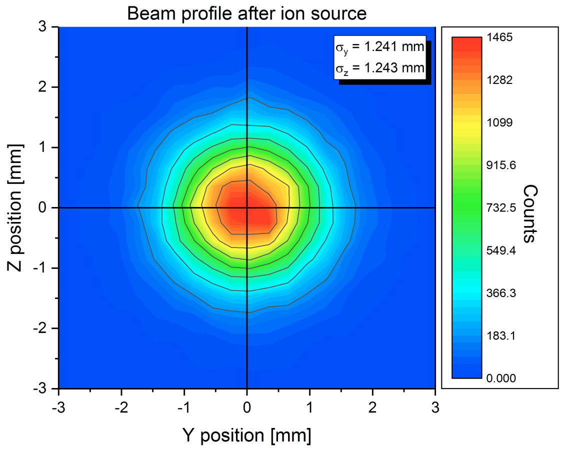

(a) Beam profile after ion source

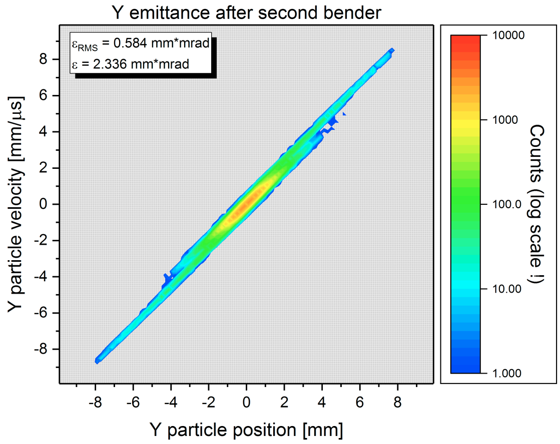

(b) Emittance after ion source

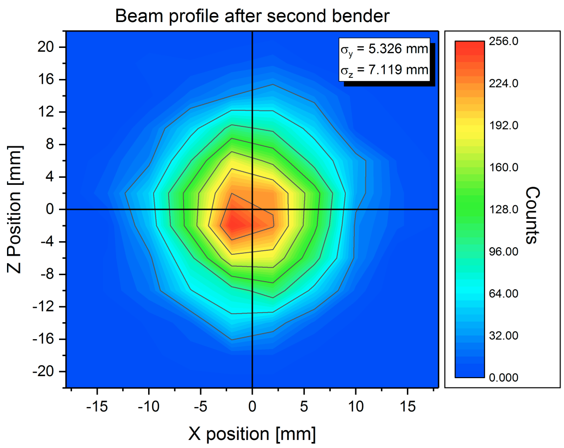

(c) Beam profile after second bender

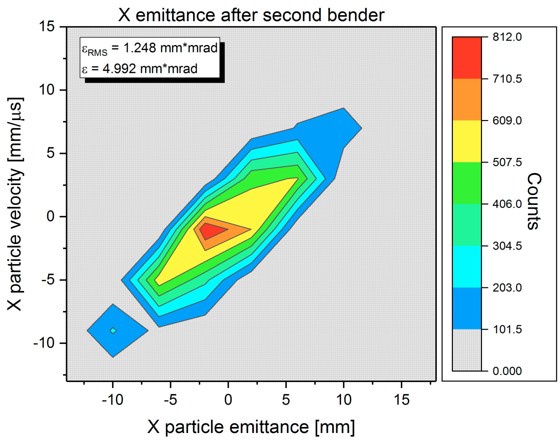

(d) Emittance after second bender

Figure 10: Result of the optimizer for the beam leaving the ion source (top row) and after the second bender (bottom row). The beam is symmetric after the ion source but diverging, with given voltage restrictions the einzellens is not able to focus it sufficiently. After being bend twice the beam is asymmetric and more narrow in the dimension of the bender and kicker. Axis declaration: x-axis (beam axis), y-axis (bender and kicker), z-axis (horizontal axis).

electrode optics and it seems that the bending has some focusing effect, the size is $\sigma_y = 5.3\,\text{mm}$.

Vertical beam line

After the last bender the ions have to cover roughly three to four meters before reaching the catcher foil. In this part of the simulation the optimizer and the random search only looked for maximizing the current received on the target itself since there will not be any further transport.

In total seven different drift tubes, two retardation electrode and one einzellens electrode was available for transporting the beam.

Since the parameter space was too large (ten electrodes) the beam transport re-

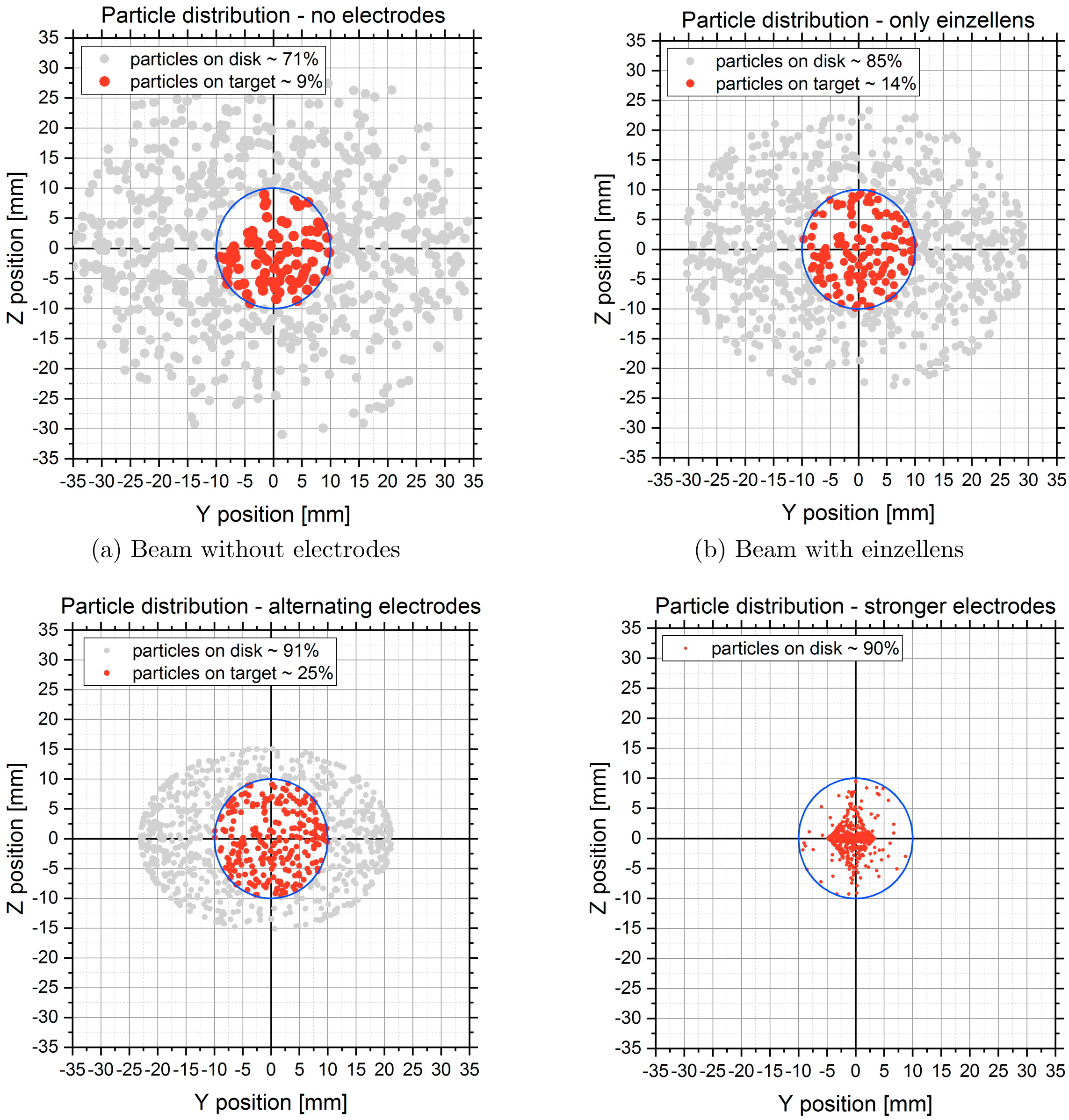

(a) Beam without electrodes

(b) Beam with einzellens

(c) Beam with alternation electrodes

(d) Beam with stronger electrodes

Figure 11: Result for the vertical beam line: a test was carried out with electrodes turned off, only the einzellens turned on, alternating electrodes, and stronger alternation electrodes. The particle distribution is shown at the location of the lower detector disk. The blue circle denotes the hole for the beam, the gray dots stand for the particles stopped by the disk, and the red dots for the particles actually received on the target foil.

sult was tested with four scenarios: no electrodes turned on, only the einzellens turned on, alternating electrodes, and alternating electrodes with higher voltages than available. This approach was chosen to contrast each case and to show what is needed to get a good transport in the last beam line part.

In figure 11 the results are shown. The top left panel shows the beam profile on the bottom side of the lower detector disk: since the beam has to pass through a

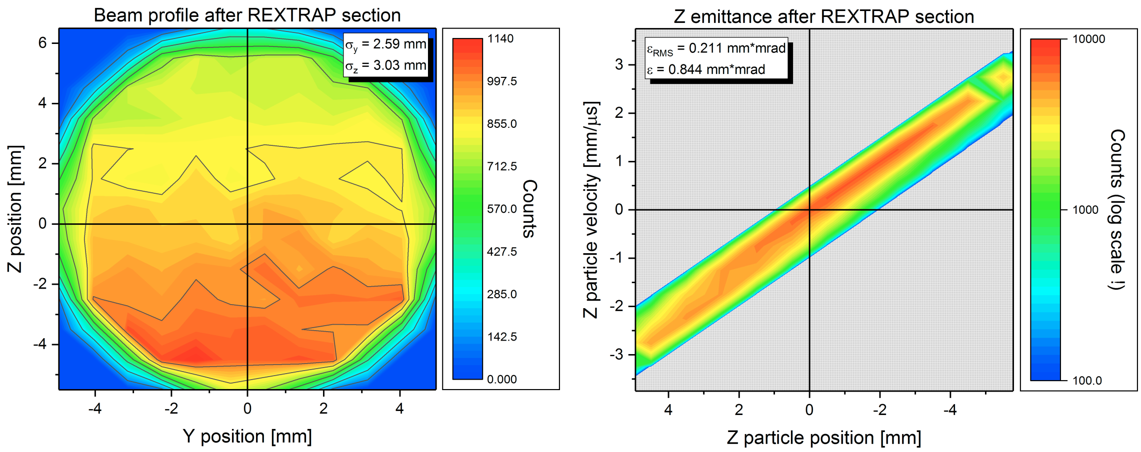

(a) Particle distribution

(b) Z emittance

Figure 12: Result for the REXTRAP beam line section.

circular hole with a diameter of two centimeters to get to the catcher a small beam is necessary. When no electrodes are turned on only 9% of all particles reach the target, the beam is diverging.

If the einzellens is turned on with maximum power then the beam is slightly focused (top right panel) but still 85% particles are lost.

Turning on all available electrodes to maximal power did not lead to an improved transport. Turning on only every second electrode gives a similar behavior as using multiple einzellenses in series and increases the efficiency to 25% which is the maximum for the given voltage limits (lower left panel). Using the same alternating setup and stronger electrodes one can get very good efficiency with a transport of about 90% (lower right panel).

REXTRAP beam line section

After the ion beam coming from the offline ion source was simulated the beam line part connecting the horizontal beam line and the REXTRAP beam line was constructed. The beam from ISOLDE is guided through REXTRAP and arrives in a roughly two meter long connector piece where the beam is bend by 29° in the horizontal plane. To achieve this, a kicker and a bender is used. Another einzellens is located behind the bender (for more details see figure 18). The results are presented in figure 12. The beam is centered but Gaussian distributed only in the vertical dimension. The horizontal dimension is shifted towards one side of the beam line. This might be due to the kicking and bending process that happens in this plane. The emittance also shows that the einzellens is not strong enough to significantly focus the beam therefore the beam is diverging to a certain degree.

3.2 Detector characterization studies

The detector tower of the WISArD experiment is equipped with eight surface-barrier silicon detectors, a plastic scintillator with photo diode readout, and several tem-

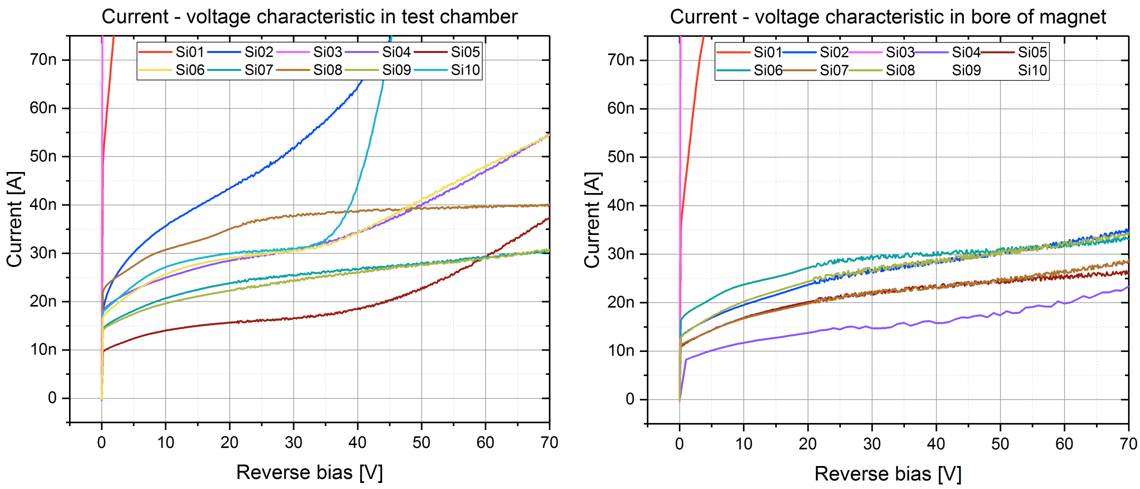

(a) Test chamber measurements (b) In bore measurements

Figure 13: Current-voltage characteristics for the ten (eight) silicon detectors. Left: test in the small chamber with all ten detectors, right: test of eight detectors installed in the bore of the magnet.

perature sensors to monitor the temperature of the detectors. In this section, the current-voltage characteristics of the silicon detectors were examined, the energy resolution of a single silicon detector was measured, and two temperature sensors were installed.

I-V characteristics

The current-voltage behavior of ten available detectors was measured using a Keithley sourcemeter controlled by a LabVIEW program.

In a first step each detector was tested separately in a small vacuum chamber for light tightness. The result is shown in Fig. 13. The behavior of the detectors can roughly be split into four groups: the first shows very high current in the low voltage region (Det01 and Det03). The second group (Det07, Det08, and Det09) shows a slow and steady increase between 20 V and 70 V. The third group (Det04, Det05, and Det06) shows similar behavior as the second group but increases in slope around 35 V. The other two detectors (Det02 and Det10) are not similar to any other detector and form the forth group.

In a second step eight of the ten detectors were installed in the bore of the magnet which was neither cooled nor energized and therefore at room temperature. The result is shown in the right panel of Fig. 13. In this measurement only two different behaviors appear: detector one and three still have very high currents at low voltages, but detectors three to eight now show very similar curves.

The difference between the two measurements can probably be found in the unstable temperature conditions of the small chamber. Since the detectors had to be tested one after each other the temperature fluctuations might have affected the current flowing through the semiconductors.

The difference between the high-current behavior of detector one and three and the

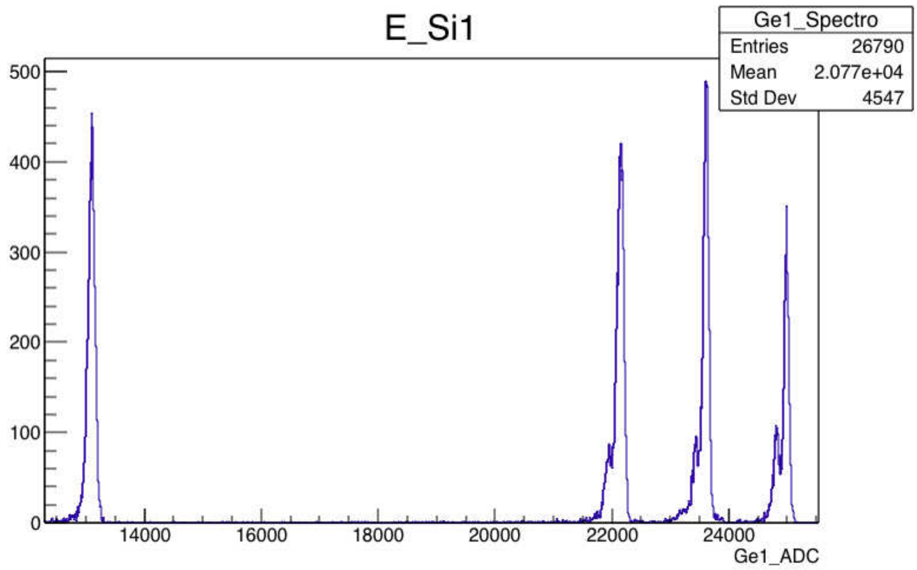

Figure 14: Energy spectrum of a mixed alpha source measured with one of the silicon detectors. The vertical axis shows counts in arb. units, the horizontal axis the not yet calibrated ADC channels. Plot from V. Araujo-Escalona.

other detector could be the result of a different layer thickness of the detectors where a smaller layer size would result in an overall higher current. Further, a different bonding between silicon substrate and copper contact could also lead to varying currents. Nevertheless it is assumed that all detectors have the same layer thickness therefore the reason for the different characteristics is not understood besides the given possible explanation.

After measuring detector nine and ten in the magnet with more stable conditions it was decided that eventually detector one and three will be excluded from the set of detectors used in the final experiment.

Energy characteristics

The energy resolution was tested exemplary with one of the silicon detectors in a small test chamber. The detector was mounted and placed above a mixed alpha source (^{148}Gd, ^{239}Pu, ^{241}Am, ^{244}Cm) within the chamber and a primary vacuum was pumped allowing the alpha particle to reach the silicon detector. The raw signal of the detector was fed through a flange and amplified by an pre-amplifier and finally digitalized with the FASTER DAQ [8].

The resulting energy spectrum is shown in Fig. 14. One can clearly see the four alpha-peaks of the mixed source and furthermore the first fine structure peak is resolved for americium, curium, and polonium. The energy resolution in this setup is roughly 50 keV. This can be improved in further measurements by optimizing the detector biasing, temperature, and data acquisition settings.

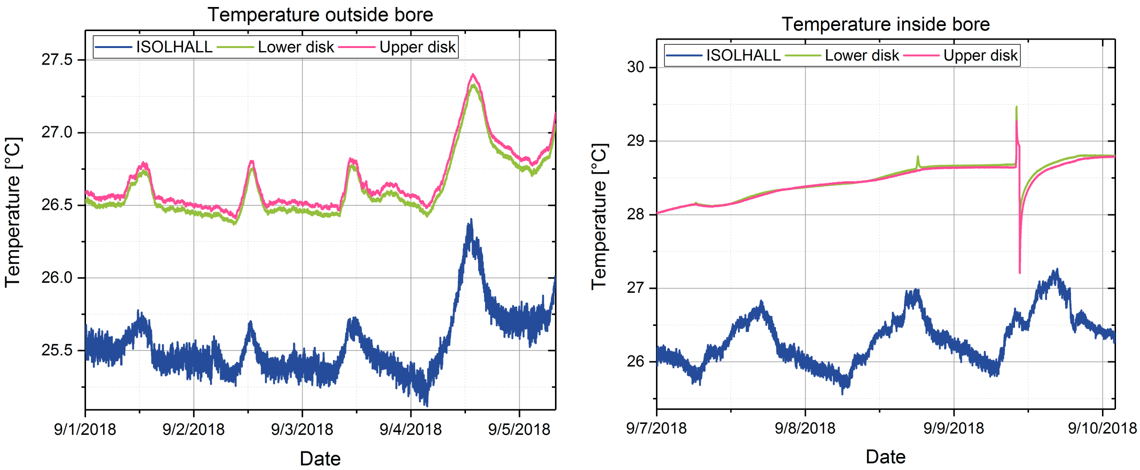

(a) Test chamber measurements

(b) In bore measurements

Figure 15: Temperature measurements with PT100 temperature sensors glued to two silicon detectors outside the magnet (left) and inside the magnet (right).

Temperature sensors

In order to get information about the temperature in the cold bore of the magnet PT100 platinum elements were installed. Two detectors were equipped with one sensor each, one on the lower and one on the upper disk by gluing them with vacuum friendly glue. The readout was done by a PICO 104 data logger. The results for a short measuring period inside the magnet and outside the magnet is shown in Figure 15.

In both cases the blue curve shows the ambient temperature of the experimental hall measured by a sensor only exposed to air. One can clearly see the day-night night cycle. The green and pink curves show the temperature of the two sensors in thermal contact to the detector PCB's. Outside the magnet the day-night cycle is visible as well but putting the detector tower with the sensors in the magnet and pumping vacuum this can not be found anymore. Instead it seems that the detectors slowly heat up by roughly one degree. This might be due to lack of heat exchange with rest gases and the cooling system not turned on yet.

4 Summary and Outlook

The simulations performed for getting good values for the ion optics yielded diverse results. The ion source seems to work properly but the given maximal voltages for the ion source appear not to be strong enough to focus the beam properly for the following beam transport. The beam transport after the ion source bender through the horizontal beam line is sufficient with given electrodes but without focusing elements the beam keeps on diverging. After the second bend into the vertical beam axis most ions are lost if the transport electrodes are not turned on. With given voltage constraints only 25% of the beam is received on the catcher foil when the electrodes are turned on with maximal voltage in alternating configuration. The overall beam transport and collection efficiency might be increased by using stronger power supplies for the einzellenses.

After finishing the optimization for the off-line ion source beam also the REX-TRAP beam line part was simulated. It was found that the beam profile is asymmetric in the horizontal plane and that the einzellens is not strong enough to focus the beam to avoid further divergence.

Further, studies for the silicon detectors were carried out. A voltage sweep to measure the current-voltage behavior showed typical temperature dependencies of the silicon detectors and after measuring under more stable temperature conditions inside the magnet it was found that two detectors show much higher currents for lower voltages than the other tested detectors. Out of ten available detectors tested, only the eight detectors with most similar current-voltage characteristics will be used in the final setup.

An exemplary energy spectrum of a mixed alpha source was taken with one silicon detector in a small test chamber. The detector was able to nicely resolve all four peaks of the mixed source and was able to show the first peak of the fine structure splitting. The energy resolution without cooling and further signal optimization in the acquisition system yielded about 50 keV.

Temperature sensors were installed to monitor the temperature of the silicon detectors in the cold bore of the magnet. A test outside the magnet showed that the sensors, even though not yet calibrated, show the same temperature for both detectors on air. Inside the magnet they showed that, when vacuum is pumped, the temperature slowly increases and eventually saturates.

The simulations will be used to compare manual beam tuning settings with simulated and decide for a final set of parameters to choose from. The current-voltage characteristic test led to the decision to exclude two detectors and only use the eight most similar in the final experiment. The temperature sensors will be used to monitor the temperature of detectors and preamplifiers in the magnet.

Acknowledgments

In this section I first want to thank my supervisors Dinko and Victoria for their amazing efforts and multiple hours spent explaining various theoretical and technical aspects of the experiment and in the lab. They not only taught me as a summer student but also embraced me as a fully responsible team member in the group. Also outside of CERN they always supported me in various situations which a summer student can encounter. Again, many many thanks.

I also want to thank all my colleagues at ISOLDE I worked with, especially Frank Wienholtz and Maxime Mougeot who helped me when I encountered problems in the `LUA` programming part. Also much appreciation for allowing working in the ISOLTRAP office which made life and programming much easier.

Lastly, I want to thank CERN's summer student team who have organized many visits of CERN's facilities and other workshops which was a great opportunity to partake in. Further, my gratitude goes out to all my fellow summer students which made this summer in an international community one of the most awesome and stimulating summers a young physicist could hope for.

References

[1] K. Heyde. *Basic Ideas and Concepts in Nuclear Physics.* Institute of Physics Publishing, Second edition, 1999.

[2] K. S. Krane. *Introductory Nuclear Physics.* John Wiley & Sons, Corvallis, Oregon, 1988.

[3] N. Severijns, M. Beck, and O. Naviliat-Cuncic. Tests of the standard electroweak model in nuclear beta decay. *Reviews of modern physics, volume 78*, July-September 2006.

[4] Nathal Severijns. *Weak Interaction Studies by Precision Experiments in Nuclear Beta Decay.* Springer-Verlag Berlin Heidelberg, 2004.

[5] Adelberger et al. Positron-neutrino correlation in the 0+ 0+ decay of 32Ar. *Physics Review Letters, Volume 83, Number 7*, August 1999.

[6] M. Beck et al. Witch: a recoil spectrometer for weak interaction and nuclear physics studies. *Nuclear Instruments and Methods in Physics Research A 503 (2003) 567-579.*

[7] E. Piselli and A. Akroh. New CERN Proton Synchrotron Beam Optimization Tool. *16th Int. Conf. on Accelerator and Large Experimental Control Systems 2017, Barcelona, Spain, JACoW Publishing.*

[8] LPC Caen. FASTER Data Acquisition. Retrieved online: `http://faster.in2p3.fr/`, September, 2018.

[9] R. Dominguez-Reyes, N. Adimi, M. Alcorta, A. Bey, and M.J.G. Borge et al. Detailed beta-decay study of 32Ar. *Submitted to J. Phys. G: Nucl. Phys; Experience GANIL-SPIRAL.*, 2011, in2p3-00617510.

A Supplemental information

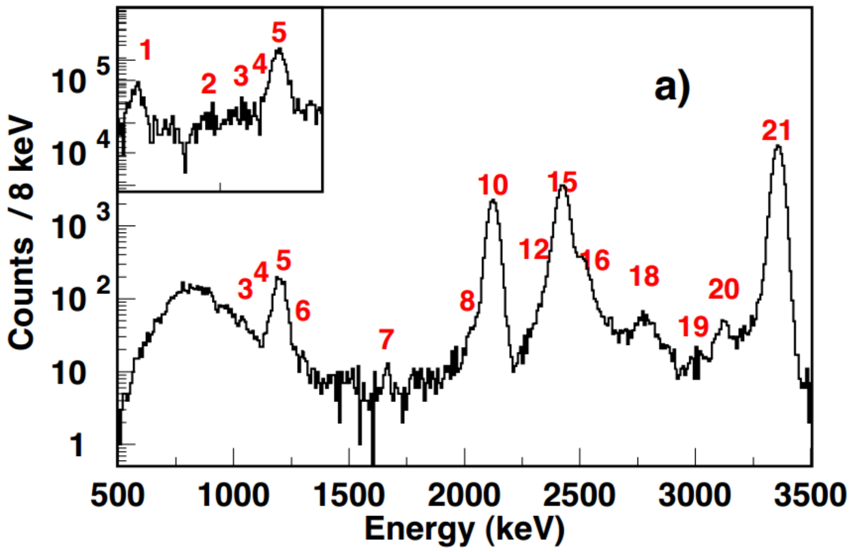

Figure 16: Energy spectrum of several proton groups resulting from the beta-delayed proton emission of the ^{32}Ar decay. The numbers label each identified group. Graphic taken from [9].

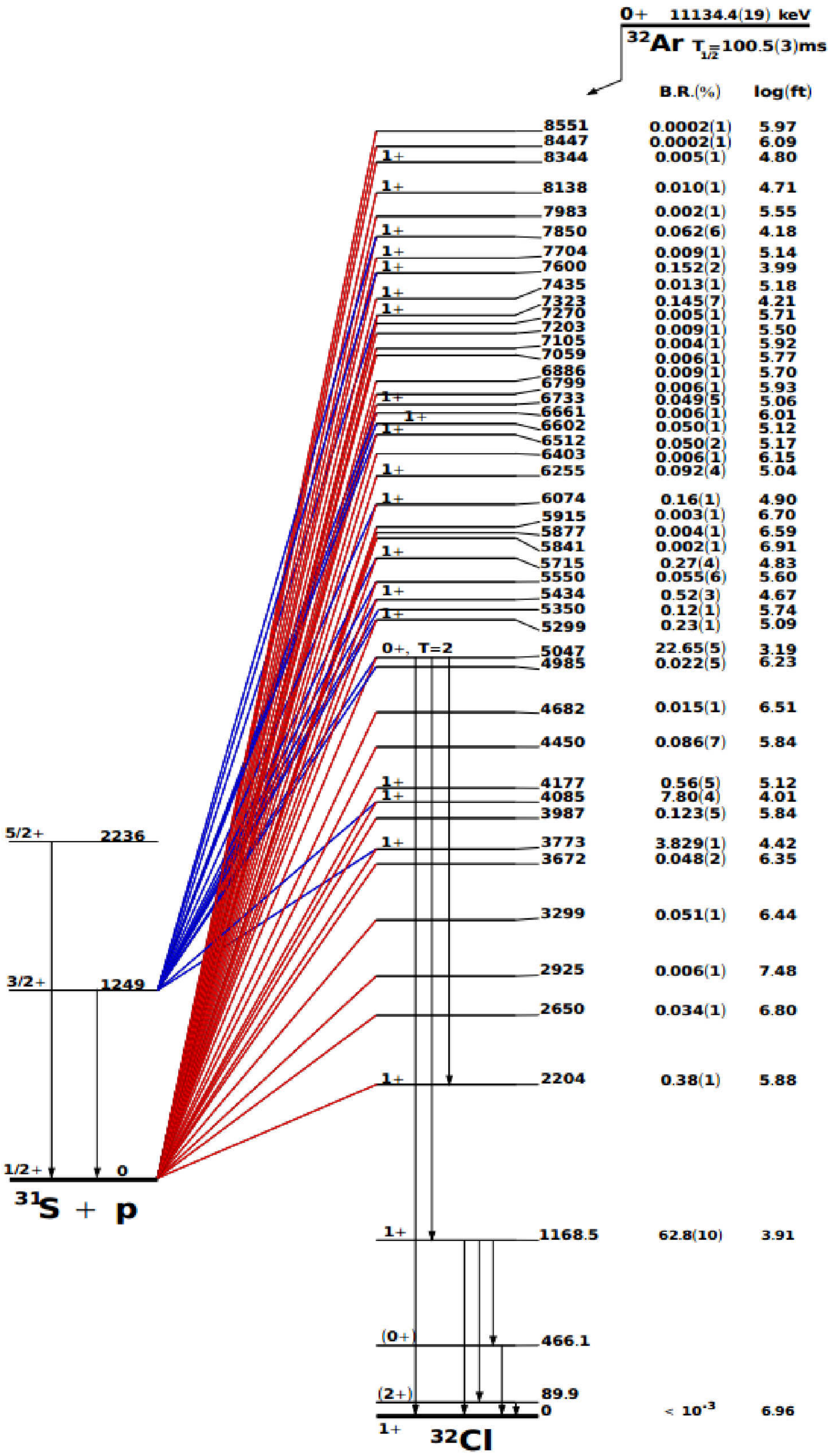

Figure 17: Energy scheme of the beta-delayed proton emission from ^{32}Ar decay to ^{32}Cl and ^{31}S. The transition with the largest branching ratio ($\approx$ 22.65%) is the super-allowed decay with $T = 2$. Graphic taken from [9]

.

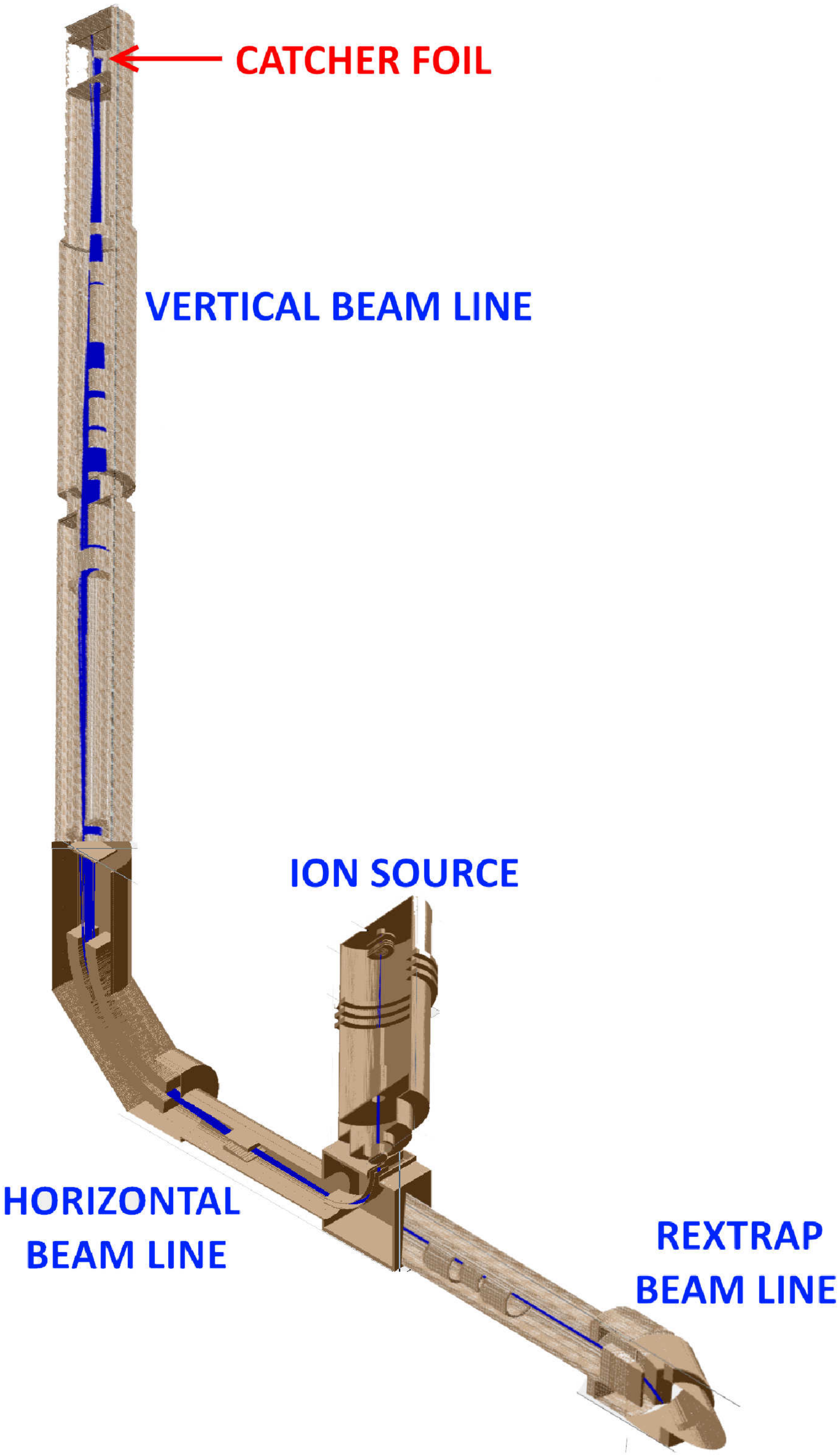

Figure 18: Visualization of the beam line simulation with SIMION. The four parts are the vertical beam line, the horizontal beam line, the connector beam line to REXTRAP, and the ion source.

.